GSCAN

PUBLIC PROCUREMENT NO. 255212 “PURCHASE OF ADDITIONAL STUDIES FOR IMPACT ASSESSMENT”

REPORT OF ACTIVITY 1

“The development of unique detectors for mapping the locations of the disused sealed radiation sources and radioactive waste placed in the reactor compartments and then covered with concrete”

MAJANDUS- JA KOMMUNIKATSIOONI-MINISTEERIUM

Lääne-Harju vald

KESKKONNAMINISTEERIUM

Euroopa Liit Ühtekuuluvusfond

Eesti tuleviku heaks

A.L.A.R.A. As Low As Reasonably Achievable

TOETAB

RAJALA

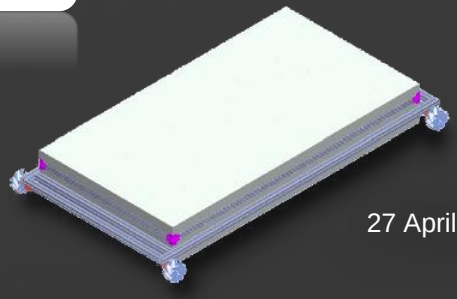

27 April 2023

GScan OÜ R&D
Tehnopargi tee 5
61715 Tõrvandi, Estonia
Reg. no. 14445579 / VAT EE102069978

AUTHORS

T.Metspalu (tarvo.metspalu@gscan.eu), M.Kiisk, M.Mikkor, M.Deak, T.Lepp, A.Ingalt, J.Štubis, M.Mägi, V.Pastsuk, F.Punga, A.Anier, K.Aktas, A.Nurme

TABLE OF CONTENTS

PROGRESS REPORT

Outline of the hodoscope measurement system development

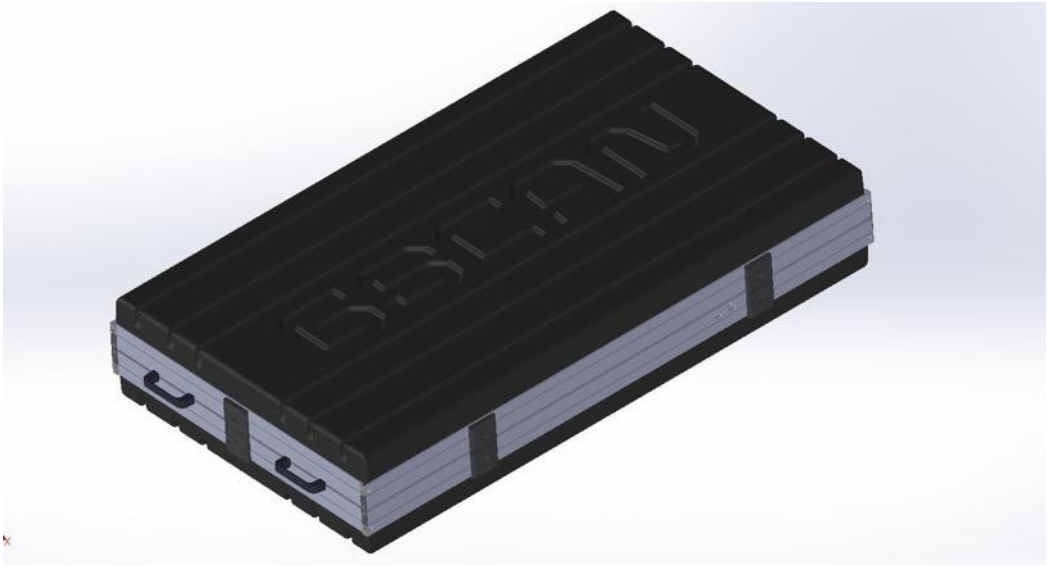

Figure 1. GScan industrial hodoscope 3D model in March 2023.

As of April 2023, two **hodoscopes** (tomographic sensor blocks) — essentially cuboids — with dimensions of **1718 x 905 x 355 mm** have been assembled**.** Each weigh **90 kg** and has a power consumption of **up to 150 W**. 3D simulations and on-site visits have confirmed that this design is optimal to be physically operated on the location.

In short, the hodoscopes will be powered through a long (ca 20 m) cable. Additional components can be either bolted onto the case and/or profiles that go around the hodoscope (see Figure 1). Data from each hodoscope will be either saved locally and then extracted manually daily or, more preferably, transferred through an Ethernet cable running in parallel with the power cable connected to the hodoscope. Wireless connection is complicated due to the specifics of the location. Technical details to follow in section 2 and 3.

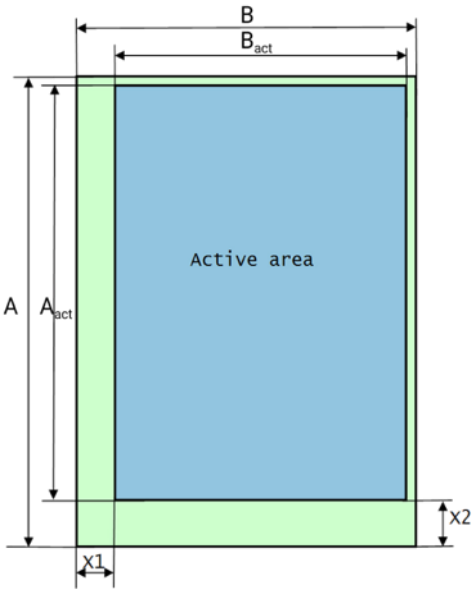

Figure 2. Hodoscope, its external dimensions A & B and an active area marked in blue.

Not the whole area of the hodoscope is able to do the measurements (see Figure 2). Therefore, in order to cover as much area for effective measurements at the survey area, registering the location and extent of the active area of the hodoscope(s) is important. Measurement plan details explained in section 4.

The following document describes the development of these unique detectors for mapping radioactive waste and other sealed sources placed in the reactor sections and then covered with concrete. This equipment will be used to carry out tomographic measurements in extreme confined spaces and thus there have been a lot of challenges that have needed to be solved. If more detailed descriptions are required, please contact the main author of this document.

1. PLANNING

ALARA Ltd is a national company responsible for the development and implementation of radioactive waste management projects, including at the nuclear facility of the former nuclear submarine training centre in Paldiski. There are two reactors that GScan is measuring in Paldiski — 346A ("Old reactor") & 346B ("New reactor"). 346A is around 7 m in diameter and 15 m in length while 346B is around 9.5 m in diameter and 12 m in length, both resting on top of a steel scaffolding supported onto concrete beams. We have created physically accurate 3D models of these locations with an accuracy of around 1 cm (see section 4). Both locations have rough concrete surfaces, confined entrances (ca 2 m in length, 0.55 m in width and 1.2 m in height) and confined working conditions in general. Details in section 4.

Maximum possible dimensions for the hodoscope have been chosen which can be transported under the reactors and operated in constrained space without damaging the construction itself. If the hodoscope were any larger, there would be many complications.

The tomographic measurements are planned to be carried out with a single hodoscope per reactor, which enables to carry out muon scattering tomography (MST), but not muon transmission tomography (MTT), where hodoscopes are placed on opposite sides of the object(s) to be scanned. MST has been chosen over MTT as it offers a bigger field of view (see section 4.3) compared to a very narrow measurement beam of MTT. This means that MST is more optimal to measure huge objects without needing additional funds and time for constructing more hodoscopes and complex infrastructure to align hodoscopes on either side of the reactors. Furthermore, MTT would require more measurement positions than MST.

On the other hand, it has to be taken into account that muon scattering tomography (MST) requires more complex data analysis than MTT. Additionally, MST typically requires long exposure times (a single measurement time per hodoscope position). At the same time, the MST method is useful for situations where a single measurement can take hours or even days as is the case with the reactors in Paldiski. Moreover, thanks to the wide field of view of the MST method, the total measurement (sum of the exposure times of all positions) takes less time in total in comparison to MTT, thus results can be obtained quicker.

Our first on-site tests provided details on how to set up the hodoscope and the measurement plan (see Table 1), where the exposures are planned to take either 48 or 72 hours per one position as the Sites can only be accessed on working days (48 h exposures start on Mondays & Wednesdays, while 72 h exposures start on Fridays). In short, the total measurement is expected to take 3 to 4 months per reactor — again, the longer the total measurement time, the better are the expected results. Details in section 4.

Table 1. Estimated measurement plan and duration

Measurement	**Measurement positions (min.)**	**Total measurement duration (approximation)**	**Starting date**
First on-site test	2	Up to 3 days	March (W13-W14)
346A reactor	39	Ca 2200 to 2800 hrs (117 days)	April (W17-W18)
346B reactor	25	Ca 1400 to 1800 hrs (75 days)	May (W18-W21)

2. HODOSCOPE PRODUCTION

2.1 FIBRE-MATS, COLLECTORS, SIPMS & MIRRORS

The bulk of hodoscope's assembly consists of fibre-mats (see Figure 3), which are produced by aligning plastic scintillating fibres (PSF) onto composite honeycomb panels.

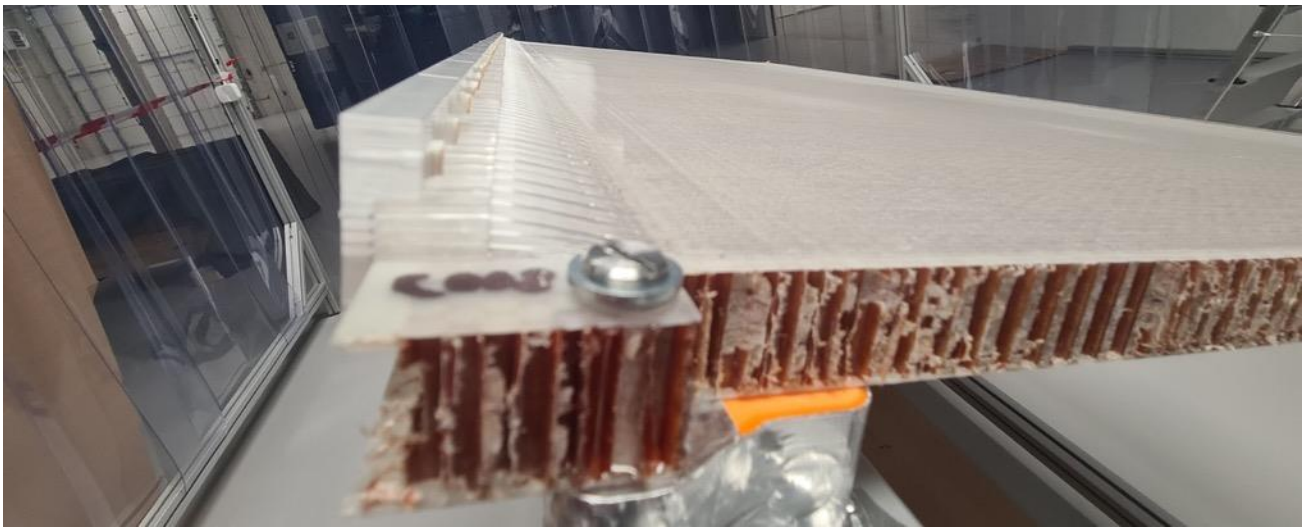

Figure 3. A honey-comb fibre-mat. From left to right, 2nd gen collectors with inserts for adjustment pins have been glued onto pre-collectors. Thereafter, 4 sublayers are guided to 2 layers of PSF.

From the end of December 2022 throughout February 2023 fibre-mats have been produced (1538x768 mm ("wide") and 768x1538 mm ("long")) to construct a hodoscope for ALARA measurements. Each fibre-mat has been fitted with pre-collectors comprising a set of splitters that pre-align the fibre-ends according to the SiPM (silicon photomultiplier) geometry (2 fibre layers into 4 sublayers of 4x4 sets). The final alignment on the fibre-mat side is done by gluing a guiding collector with conical holes onto the fibre-ends.

Six fibre-mats or three pairs of fibre-mats (3 "wide" + 3 "long") are used to assemble a hodoscope. For each pair — a detector plate — one "wide" and one "long" panel are carefully placed onto each other with fibres coming into contact perpendicularly while making sure the pressure is minimal to avoid damaging any PSF. These detector plates are thereafter distanced from one another using metal distance rods.

In general, the production can be divided into the following steps:

1) Pre-processing of the honey-comb plates (milling grooves)
2) Automated manufacturing of fibre-mats with a proprietary robotic system FiBOT
3) Mounting the collectors
4) Milling the fibre-mat ends
5) Mounting the SiPMs, mirrors and multiplexing boards
6) Assembly of detector plates & hodoscope
7) Wiring and cable routing
8) QA procedures, functionality validation & diagnostics

Mounting the collector (including the splitters) & SiPMs, which is the most critical part of the hodoscope production, came with many challenges which involved multiple direct and indirect processes and parameters including, but not limited to:

- fibre-mat groove milling accuracy and consistency;
- fibre gluing accuracy and consistency;
- splitter gluing accuracy and consistency;
- glue position and amount under the fibres and the splitters;
- vibration introduced by FiBOT and milling equipment;
- mechanical fibre damage resulting in ‘dead’ fibres;
- mechanical damage to the honey-comb panel;
- temperature, humidity, debris & dust.

As these potential sources of defects are known to us, we have managed to mostly minimize their effect on the final product through prototyping.

To create more controllable conditions for mounting the SiPMs and mirrors, a custom relocatable clean room has been designed and constructed according to widely spread solutions available on the market. The air in the clean room is filtered with a High Efficiency Particulate Air (HEPA) UL900 Filter: 99.99% efficient @ 0.3 Micron.

Inside the clean room, the fibre-mat is laid onto a custom assembly table, which allows to rotate the fibre-mat from -180 to 180 degrees allowing us to use the same assembly table for mounting both the SiPMs on one and mirror on the other side of the mat (see Figure 4).

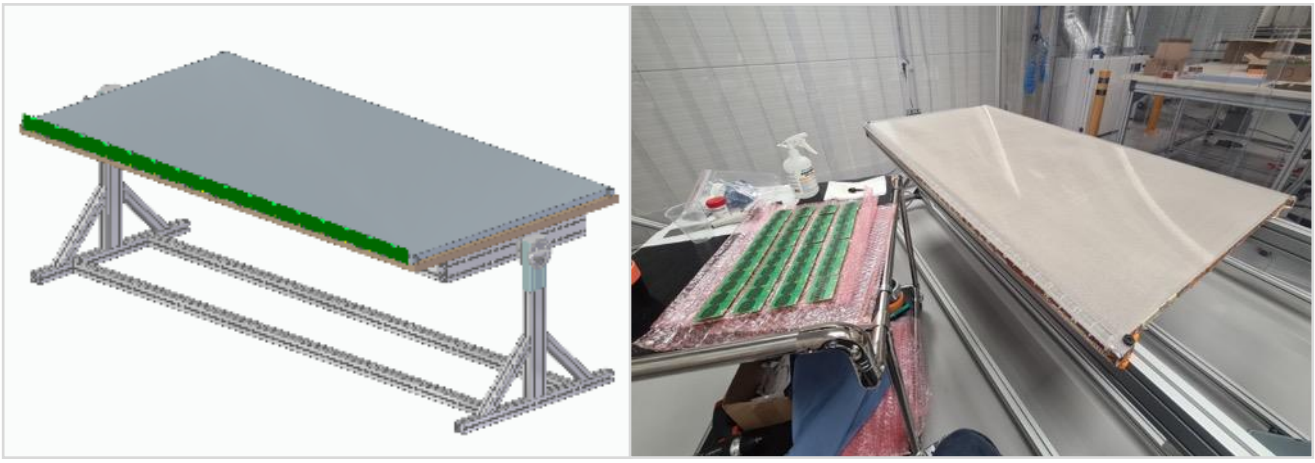

Figure 4. An assembly table inside the clean room for mounting SiPM arrays and mirrors. The table plane can be adjusted from horizontal to vertical direction.

As not all of the photons move towards the collector into the SiPM array, but in the opposing direction, mirroring materials have been tested in order to increase the general efficiency of the fibre-mat. As it can be seen from Figure 5, this has been experimentally confirmed and thus adding mirrors has become a crucial part of the production process. Currently the mirrors are mounted manually, which provides satisfying results.

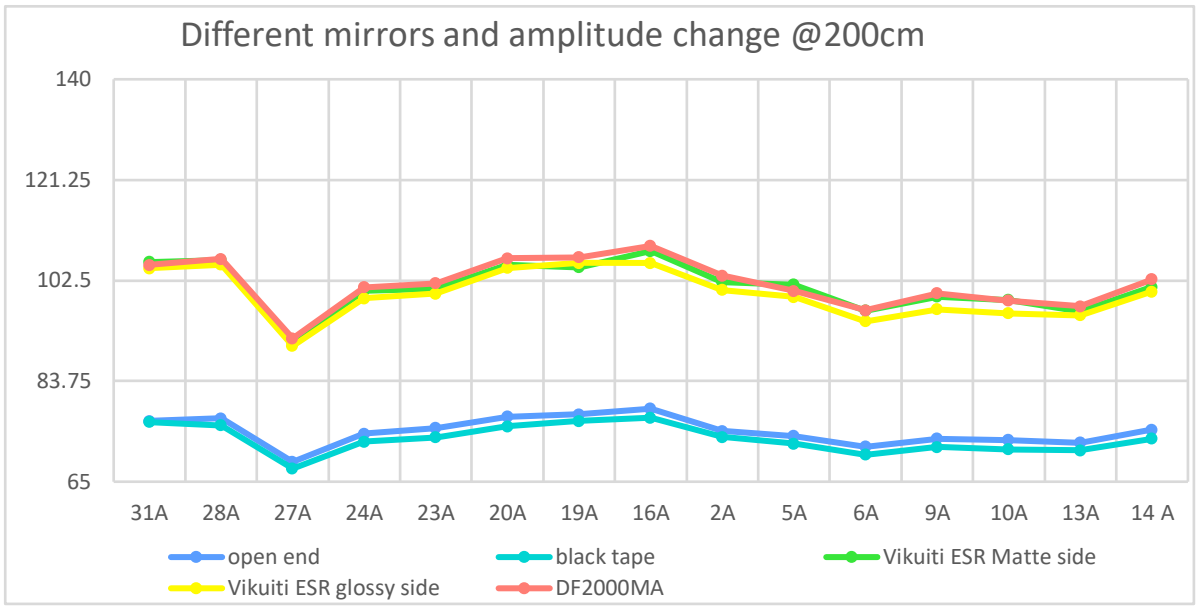

Figure 5. Comparison of signal amplitude (on the y axis) measured from the collector in different SiPM channels (on the x axis) according to the (mirroring) material used at the opposite side of the fibre-mat.

Taking all of minor production-related quality issues into account, we have maximized the efficiency of the fibre-mats that have been produced so far. In general, we have overcome the challenges with plastic scintillating fibres' placement and these have not drastically affected the efficiency of the fibre-mats already produced.

2.2 ASSEMBLY OF DETECTOR PLATES & HODOSCOPES

As can be seen in Figure 6, a demo hodoscope was assembled to test the mechanics, electronics and software of the system. In the figure, positioning distance rods have been used to position fibre-mats into detector plates and the latter into hodoscopes, which are also used for the full-scale hodoscope. This part of the assembly can already be done outside of the clean room on a sufficiently big and stable flat horizontal surface.

In addition to 'dead space' introduced in figure 2, electronics and cabling are taking away extra space that is not used for sensing purposes. Again, this area (marked in green in Figure 2) has been minimized as much as possible in order to preserve as much mobility of the hodoscope as possible. The active area is placed into one corner of

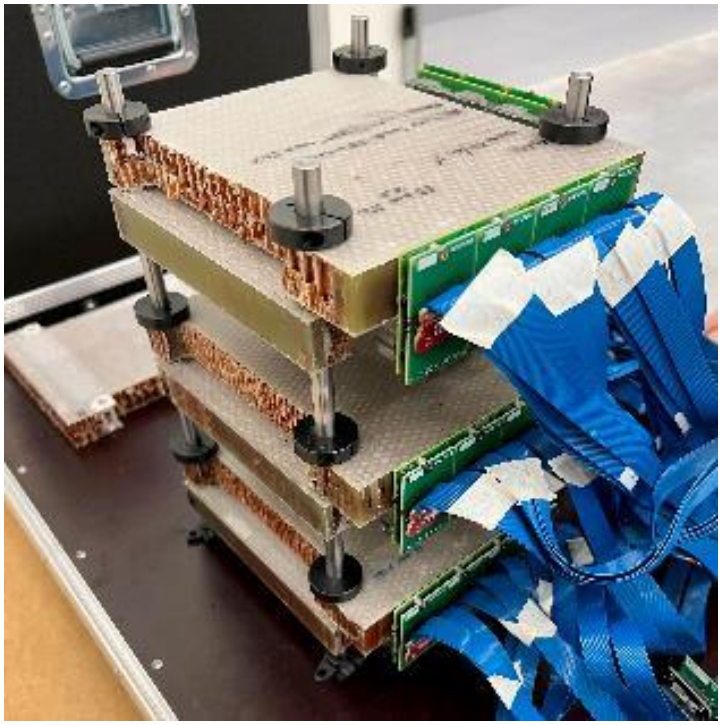

Figure 6. A demo hodoscope assembled with distance rods and container rings. Also notice green SiPM-array PCBs with corresponding blue ribbon data-cables.

the hodoscope to enable measuring the site's corners with maximum efficiency.

Finally, the hodoscope is sealed into a light protective plastic casing (see Figure 1), which isolates the sensitive sensors and electronics from external (UV) light sources, dust, humidity and significantly reduces potential physical damage to the device. The enclosure itself does not affect the measurements as the measurement process itself begins at the first PSF layer.

2.3 QA PROCEDURES & DIAGNOSTICS

Throughout the production process quality assurance (QA) has been done on every step of the way, including visual inspection, microscopic imaging, thermal and mechanical testing, mechanical tolerance measurements etc. Systematic detail-oriented procedures have enabled us to optimize the FiBOT (GScan fibre-laying robot) operational parameters and modify the design of additional details (e.g., collector) on the go. Detailed mechanical analyses are not added to this report to stay within the scope — main takeaways have been implemented in the final product.

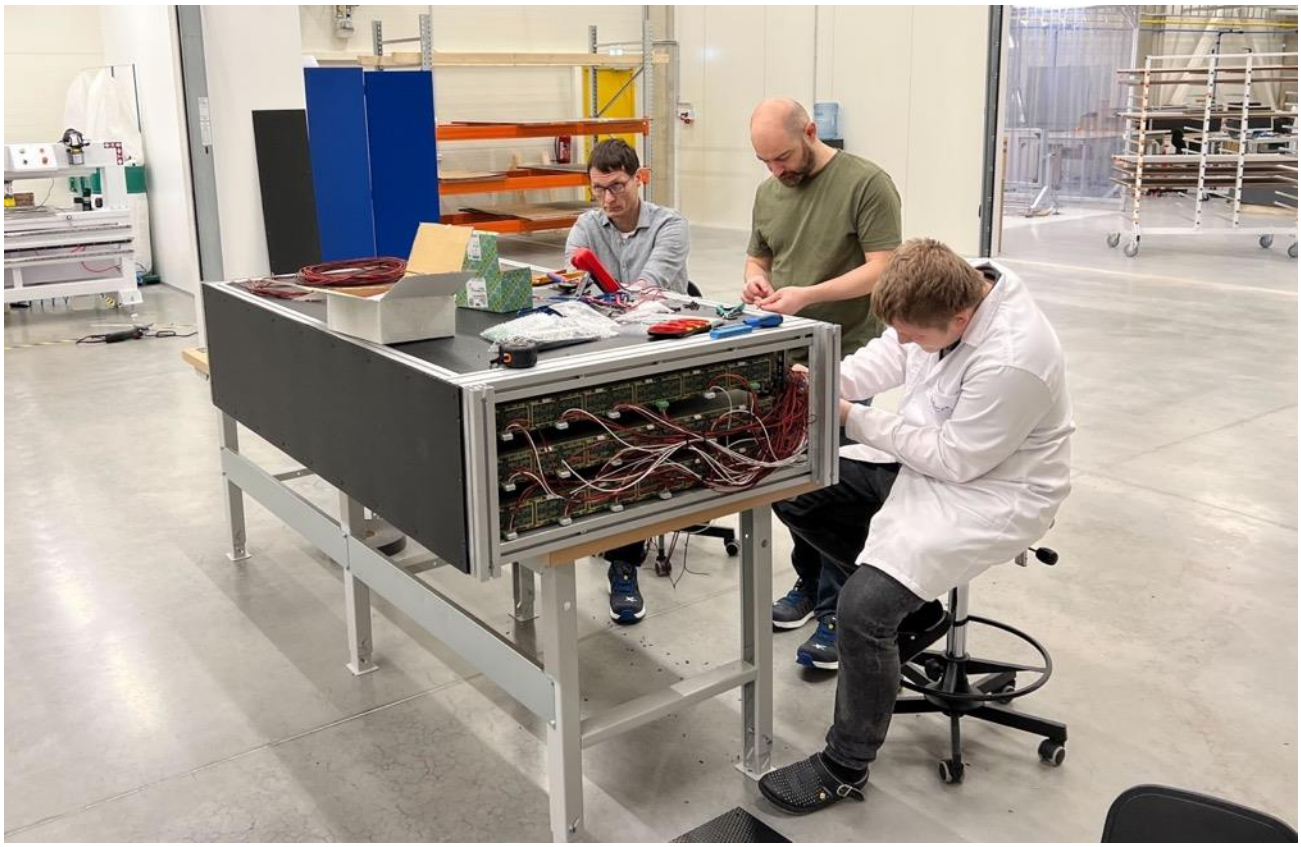

Figure 7. Full-scale hodoscope assembly: cabling and checking multiplexing connections.

3. FUNCTIONALITY TESTS

3.1 BACKGROUND INFORMATION

3.1.1 Multiplexing

To reduce the number of readout channels from the hodoscopes, an effective technique is to employ charge division (or sharing) multiplexing networks to modulate the input charge collected from the SiPM arrays. This technique routes the input charge towards output channels, and the impedance between the input channel and each of the multiplexed output channels divides the amount of input charge. As a result, the SiPMs' position and count rate information can be encoded. Typically, resistive chains are used to implement the charge division multiplexing network, which is followed by signal shaping and amplification stages at the front-end electronics module.

The hybrid symmetric charge division (SCD) network approach combines a row-column summing readout circuit (RCSRC) with a one-dimensional (1D) resistive chain or a weighted summing circuit (see Figure 8).

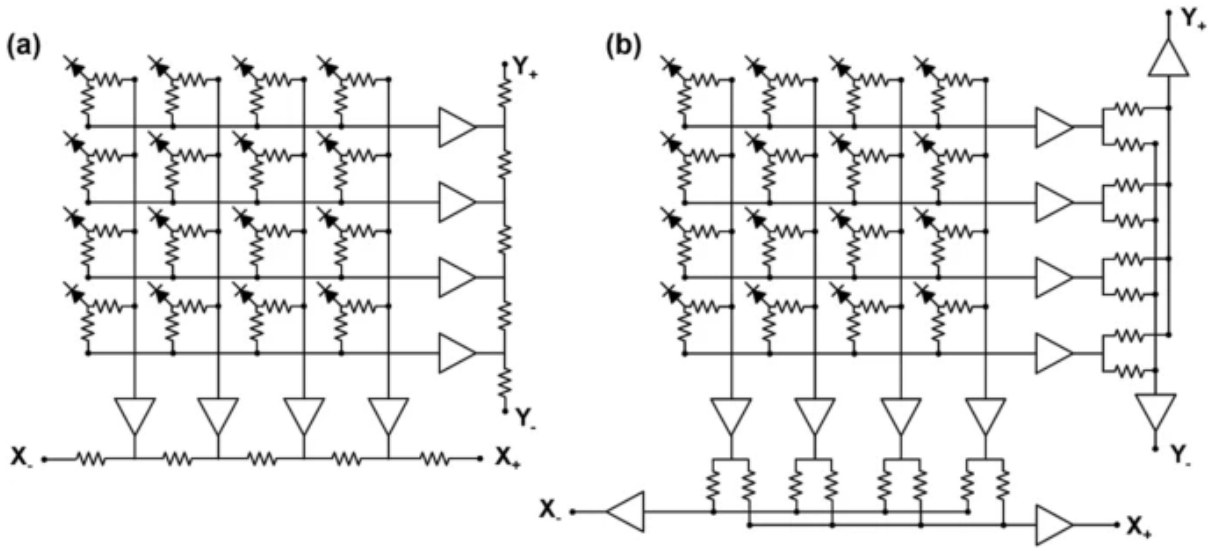

Figure 8. Simplified schematic of a 4x4 (16) SiPM symmetric charge division (SCD) network using: (a) 1D resistive chains ('ladders') or (b) weighted summing circuits.

In our R&D activities we are using a SiPM grid with twice the size. This means that with either diode or resistive symmetric charge division, 64 SiPMs (inputs) are clustered into 8 row channels and 8 column channels — 16 output channels in total, giving us a 64:16 or 4:1 multiplexing ratio. Each of these eight outputs is thereafter guided into a resistive encoding 'ladder' or a weighted summing circuit through op-amps, as seen in figure 3, producing 2 encoding outputs per 8 channels (XPLUS (X+) and XMINUS (X-) for row channels, YPLUS (Y+) and YMINUS (Y-) for column channels).

Final output channels are determined by applying the following ratio formula on outputs:

$$X_{\text{position}} = \frac{X_+ - X_-}{X_+ + X_-}, \qquad Y_{\text{position}} = \frac{Y_+ - Y_-}{Y_+ + Y_-}. \tag{1}$$

This formula outputs values between -1 and 1. Determining which channel output corresponds with which ranges will make it possible to detect which row or column channel provided the signal (see Figure 9).

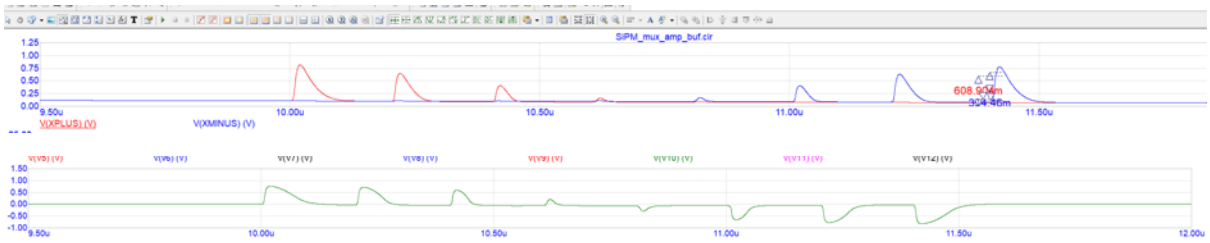

Figure 9. Above. resistive encoding outputs. Red is XPLUS (X+) and blue is XMINUS (X-). Below, formula output. Each peak determines a different channel.

By combining these encoding outputs obtained from X and Y, the measurements from each SiPM can be represented on a simple 2D graph as depicted in Figure 16 (left). Notice how each SiPM cluster can be distinguished with only 2 axes (64 SiPM arrays -> 16 row/column channels -> 4 encoding channels -> 2 ratios, i.e., 64:4 or 16:1 ratio).

In short, there are a lot of parameters that need to be set and optimized in order to clearly separate the signals after multiplexing. We have produced many custom iterations of multiplexing prototype boards and have now chosen a version, which should help us maximize the output of the multiplexing electronics and minimize the amount of wiring and supportive electronics from PETsys needed for data acquisition (DAQ).

3.1.2 Particle tracking and filtering

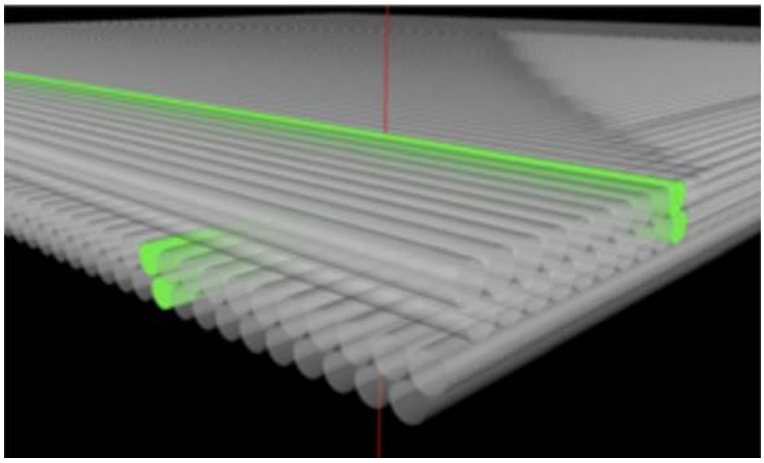

Figure 10. A snapshot from the Geant4 detector.

In order to create a 3D image of the reactor (i.e., a 3D reconstruction) using natural muon flux, trajectories of muons passing the reactor compartment have to be tracked. PSF in the hodoscope can produce light (more specifically, photons) when interacting with high-energy particles like natural muons, which can then be converted into an electrical signal by SiPMs. The read-out electronics are responsible for processing and transmitting the collected data to a recorder. The data processing algorithm is designed to search for coinciding events on multiple fibre-mats, allowing the removal of noise and non-relevant background radiation, such as gamma radiation, registered by the physical detection system. If needed, hardware changes are made after primary on-site tests to compensate for heightened gamma radiation levels.

This process ensures that only events belonging to tracks of muons and other particles (such as electrons and rare protons) with cosmic ray origin are further processed. The hodoscope design provides a tracking accuracy of approximately 100 um and an angular accuracy of about 1 mrad.

As mentioned before, the hodoscope comprises of three detector plates, each having a four-layered structure, with two double-layered fibre-mats placed orthogonally to provide the x and y position of the particle hit. The fibre diameter measures 0.9 mm, and the pitch (distance between fibres) in a single layer is 1.0 mm. The top layer of a fibre-mat has been shifted by a half pitch and aligned in an interlocked manner based on the positions of the lower layer fibres. This guarantees close to 100% geometrical detection efficiency at every angle of incidence and a high spatial resolution. A snapshot from the Geant4 (simulation package) model of the position-sensitive detector plate is shown in Figure 10, composed of two double-fibre layers placed orthogonally (represented by grey cylinders), while the trajectory of a passing muon is indicated by the red line, and the propagation is illustrated by the green fibres.

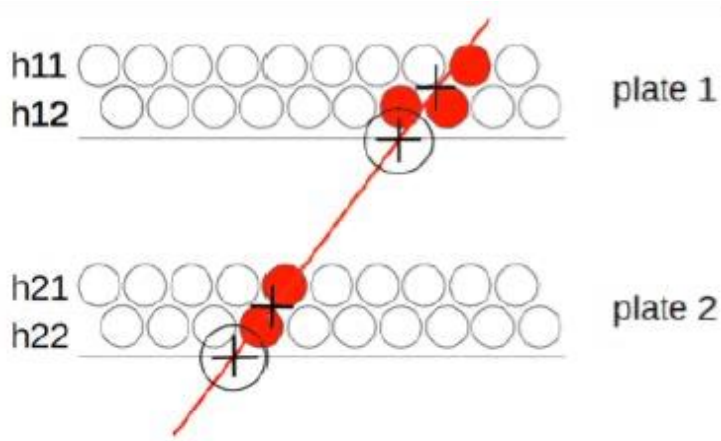

Figure 11. Muon trajectory extrapolation. The hxx represent PSF layers, red fibers represent fibers generating signal, the cross depicts the calculated particle hit coordinate, the circled cross indicates the extrapolated coordinates. Only two detector plates (instead of 3) with PSF for tracking one (instead of 2) axis are depicted.

Adding more detector plate layers, we are able to assess in greater detail where the muons hitting (going through) the hodoscope have come from (see Figures 11 and 12).

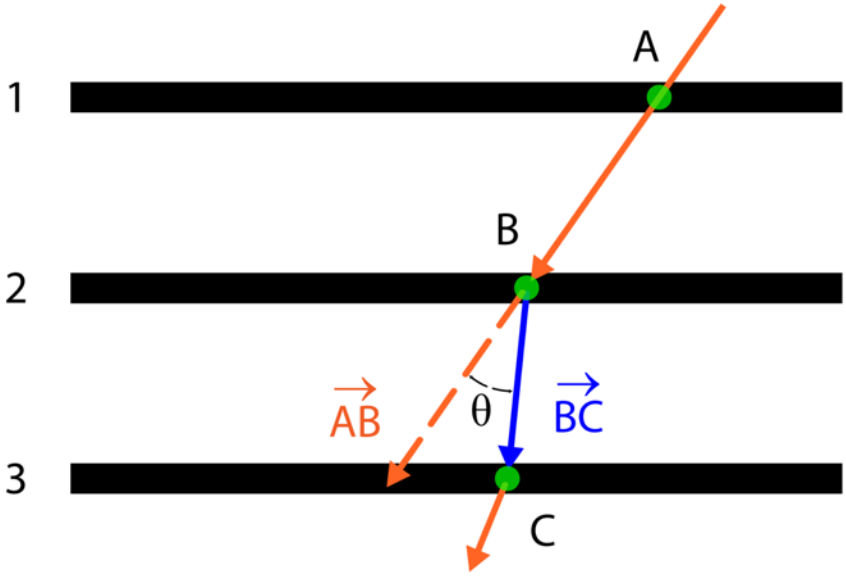

Figure 12. The intrinsic scattering angle θ we use to classify the particle events (passing muons/electrons) in the hodoscope. The hodoscope has the three detector plates (black bold lines numbered as 1, 2, 3). The arrows denote the reconstructed particle trajectory. The angle θ denotes the intrinsic scattering angle of the particle in the plate 2.

The tracking, filtering and reconstruction is described in more detail by the authors of GScan R&D team in the article “Atmospheric ray tomography for low-Z materials: implementing new methods on a proof-of-concept tomograph”, published in https://arxiv.org/abs/2102.12542.

3.1.3 Particle flux simulations

In order to simulate the passage of cosmic particles through the reactor compartments and developed detector system, we use the Geant4 software. Geant4 (for GEometry ANd Tracking) is a platform for "the simulation of the passage of different particles through matter" using Monte Carlo methods. The input to cosmic-ray modelling is taken from the best suited codes, such as CRY cosmic-ray library or Muon Parameterisation Source (MPS).

The CRY software library generates correlated cosmic-ray particle shower distributions at one of three elevations (sea level, 2100 m, and 11300 m) for use as input to transport and detector simulation codes. CRY simulation is based on precomputed input tables derived from full MCNPX (Monte Carlo N-Particle eXtended) transport simulations of primary cosmic rays on the atmosphere and benchmarked against published cosmic-ray measurements.

CRY simulation provides all particle production (muons, neutrons, protons, electrons, photons, and pions) with the proper flux within a user-specified area and altitude. The code generates individual showers of secondary particles sampling the energy, time of arrival, zenith angle, and multiplicity with basic correlations, and has user controls for latitude (geomagnetic cut-off) and solar cycle effects.

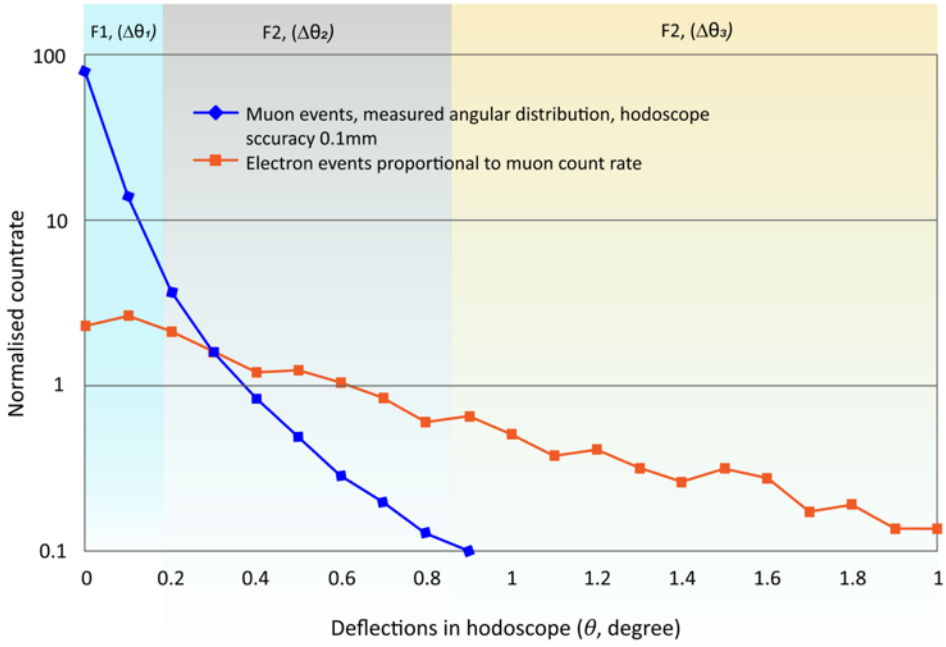

Figure 13. The distribution of atmospheric ray muons and electrons as a function of the intrinsic scattering angle θ in the hodoscope (from the Geant4 model with the CRY event generator). The distribution shows we can apply the intrinsic scattering angle θ as a discriminating parameter classifying the type and energy range of the hodoscope passing particle. The latter improves the tomographic reconstruction of scanned samples very significantly. The colored areas denote the muon and electron dominated values of θ (blue, yellow) and the mixed region (gray).

Figure 13 shows the simulation results of the filtering spectrum for the hodoscope having the distance 100 mm between the two adjacent plates. We used the CRY cosmic ray event generator to model the atmospheric ray flux consisting of muons and electrons at sea level. We fixed the spatial resolution of detector plates at 0.1 mm, which corresponds to the angular resolution of 1 mrad for particles approaching the hodoscope orthogonally. Considering the angular resolution of the hodoscope, the total spectral range presented in Figure 13 can be divided into different number of groups; we call those PTF groups below. For example, a

possible robust PTF classification schema is to classify the particle events to muons and electrons or the muons with low, medium and high momentum. In Figure 13 we have separated the spectrum into the three PTF groups: F1 (dominated by muons), F2 (mixed muons and electrons) and F3 (dominated by electrons). This classification schema has been used in the figures of the reconstruction results in the next sections.

3.1.4 Reconstruction

The hodoscope measures the number of muons that pass through it over a certain period of time (including the direction where the muon came from). If the measured flux is lower than expected, this indicates that the material above the detector is denser than expected, and vice versa. In addition, as we are able to track the trajectories of the muons, we can also estimate the location of these materials. The bigger the total hodoscope area, the better we can differentiate materials that are on top of each other.

The data files obtained from each exposure position of the detector contain activation data of channels from the DAQ electronics and metadata specifying the hodoscope location in space and exposure duration. The activation data of the channels is transformed into local xyz coordinates using a tracking algorithm that improves the trajectory of the particles through the hodoscope and removes any spurious channel activations. The tracking algorithm also applies angle filtering to eliminate low-energy particles. The exposures from all detector positions are combined into a single virtual detector plane using the hodoscope positional metadata.

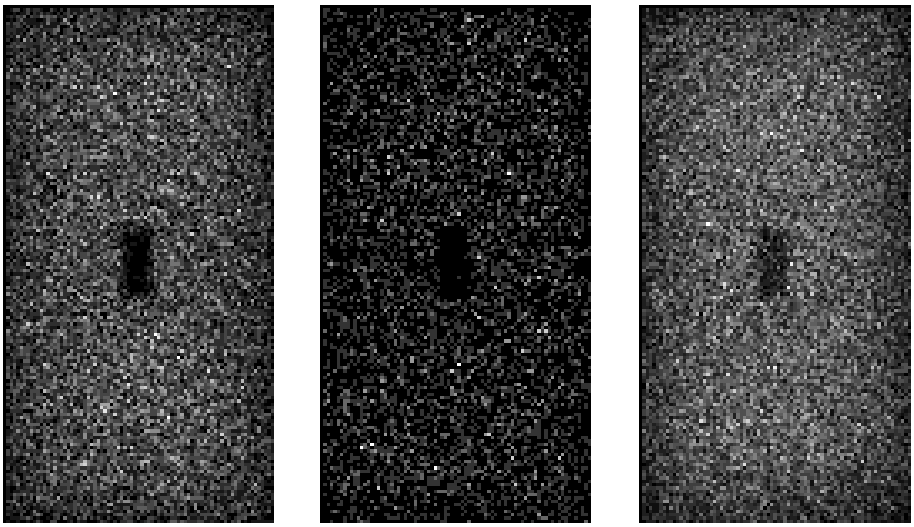

Figure 14. Proof-of-concept Geant4 long exposure simulation 2D cross-section results of the hodoscope with a lead brick on top in the middle.

The volume of interest (VOI), which is a limited space in which the submarine section is located, is divided into small space units called voxels with side lengths of either 1.5, 10, or 30 cm — the size of the voxel can be chosen after the measurements data has already been collected. The bigger the voxel size, the less time the reconstruction calculation takes. Thus bigger voxel sizes are used for quick initial estimations, as the final model will be calculated using smaller voxels. A density map of the VOI is created by projecting a ray through each voxel, and each voxel that the ray passes through is given a count of +1. The 3D density map can be presented as a 3D image or 2D cross-sectional cuts/slices where voxel ray rate, after normalization, is displayed as a pixel intensity in grayscale or coloured heatmap.

Figure 14 shows a single hodoscope's grayscale 2D cross-sectional cuts of the density map (raw images) with 1 cm voxel size at different filtering ranges produced with Geant4 particle physics simulation software package. This presents us a basis for experiments to follow.

3.2 MEASUREMENT RESULTS

3.2.1 Expected results from simulations

We have prepared a simplified model of reactor 346A in particle physic simulation software Geant4. According to our understanding, 2/3 of the compartment is filled with concrete. We have placed 5 objects of interest (specified in the technical specifications of the public procurement 'Purchase of additional studies for impact assessment') in accordance with their material and geometric characteristics into concrete (see the cross-section in Figure 15).

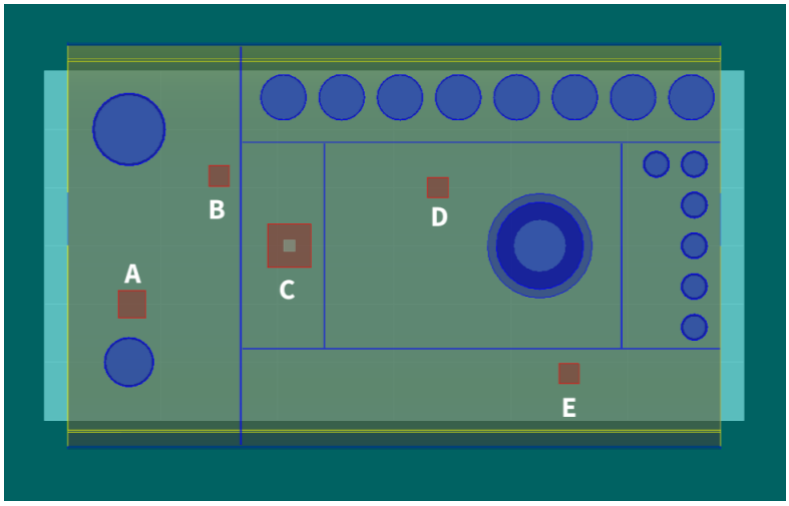

Figure 15. GEANT4 visualization of developed model of reactor compartment 1 with 5 hidden detectable objects:
A — Lead box, **B** — Plastic box, **C** — Paraffin container, **D** — Stainless steel box and **E** — wooden box.

The final measurement result at ALARA will be a 3D model of reactor sections with detected objects of interest. Additionally, we will provide cross-sectional raw data images of horizontal-cuts seen below.

We have previously run described model in Geant4 simulation with 14x14m CRY cosmic-ray library source for 2 hours of particle exposure time. Then we applied our proprietary software package to produce cross-sectional raw images (of reconstructed density map). We have used two voxel sizes 1 cm on left and 5 cm on middle and right images on Figure 17 (the cuts are taken at the height of 5 boxes).

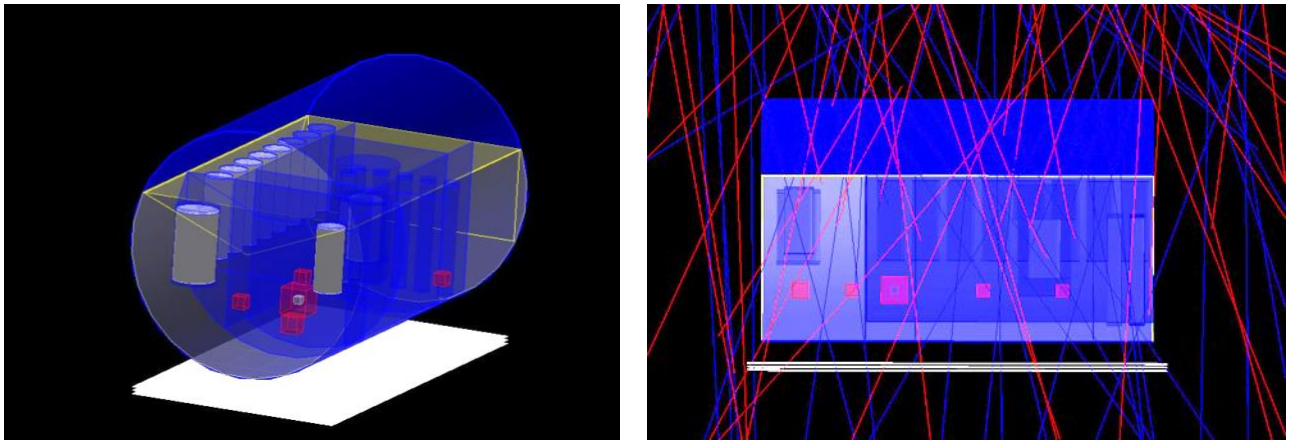

Figure 16. 3D model of reactor 346A bombarded with cosmic rays.

While it is easier to spot all five boxes on the lower resolution image in the middle (right image is same as middle image with objects of interest circled for easy spotting), we also loose

considerably detail compared to the left image. Final decision on used resolution (voxel size) will depend on measurement time available, but the voxel size will not go beyond 30 cm.

On figure 18 there are two raw cuts from different box placement scenario (cross-sectional cuts are made at the height of metal boxes) — on the top there is 2 h exposure reconstruction and below, 10 h exposure — only high energy particles were used (below 1 mrad of hodoscope internal scattering). As it can be seen, the longer exposure image provides much more sharpness and contrast due to increased statistics.

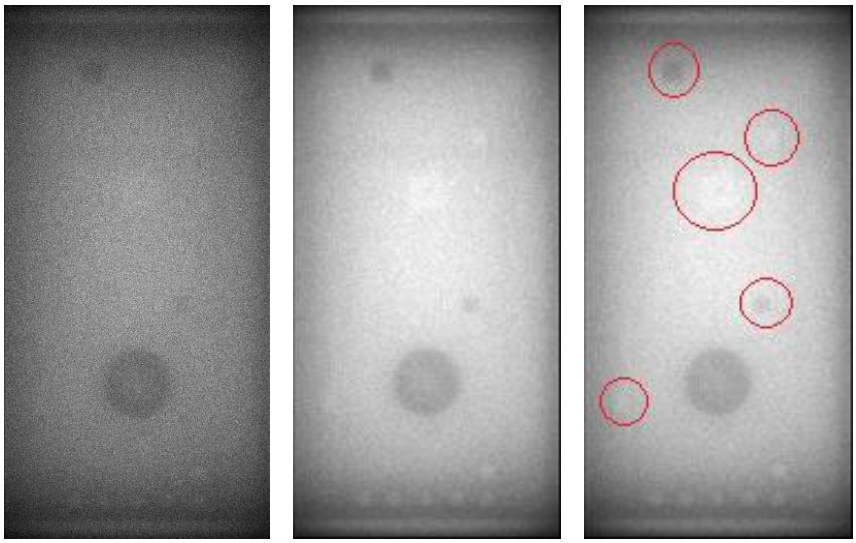

Figure 17. Two hours of exposure in the simulation — left 1 cm voxel size and middle & right 5 cm voxel size.

Based on initial simulations it is assumed that minimum of 12h of exposure is required to find objects of interest (boxes defined by procurer) and other radioactive waste, but preparations are made to extend the exposures to 72h of exposure if

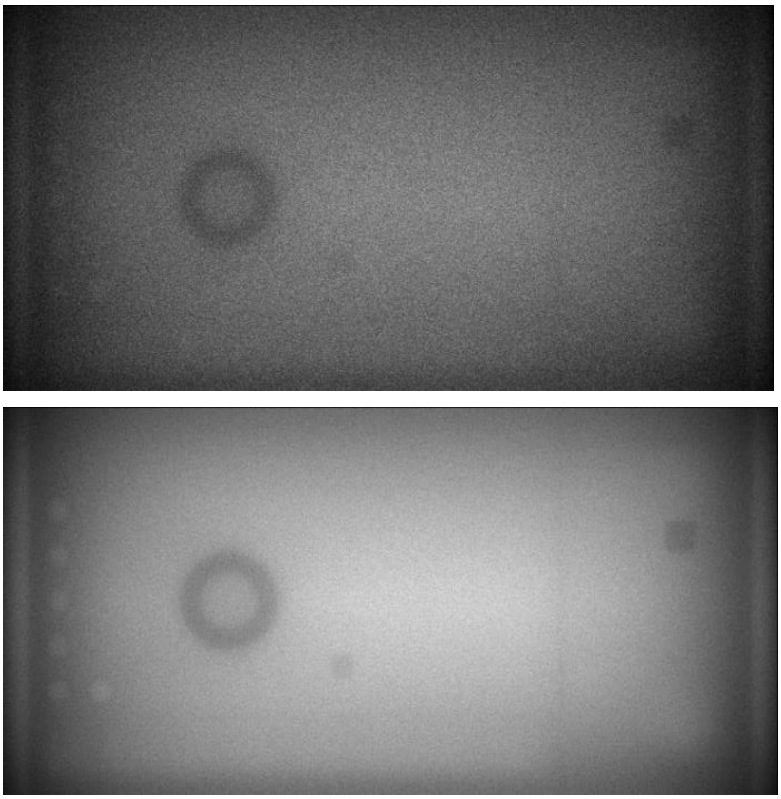

Figure 18. On the top, 2 h exposure simulation reconstruction and below, 10 h exposure. Notice the improved contrast and details of the image, which machine learning can easily analyse.

need be and provided time is available. Preliminary simulated data indicates that only one-sided limited angle tomographic transmission measurement suffices to achieve set goal.

3.2.2 Multiplexing

Each set of X+, X-, Y+ & Y- that unambiguously helps to define a hit in a specific fibre is denoted as a ‘quadruple’. Each set, which is missing at least one of these, is disregarded.

Analysing the hits from the hodoscope’s signal constellation and applying different filtering methods to remove as much noise as possible, we managed to measure the distribution of hits each multiplexing scheme received. Note the outliers in Figure 19, which gave unreliable results and were

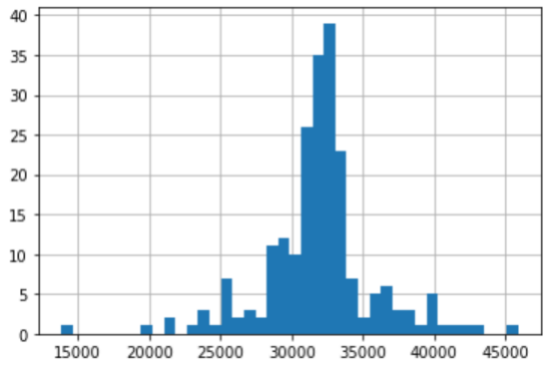

Figure 19. Distribution of muxing scheme counts (quadruples) in mux schemes. x-axis: counts of quadruples; y-axis: count of mux schemes with said counts.

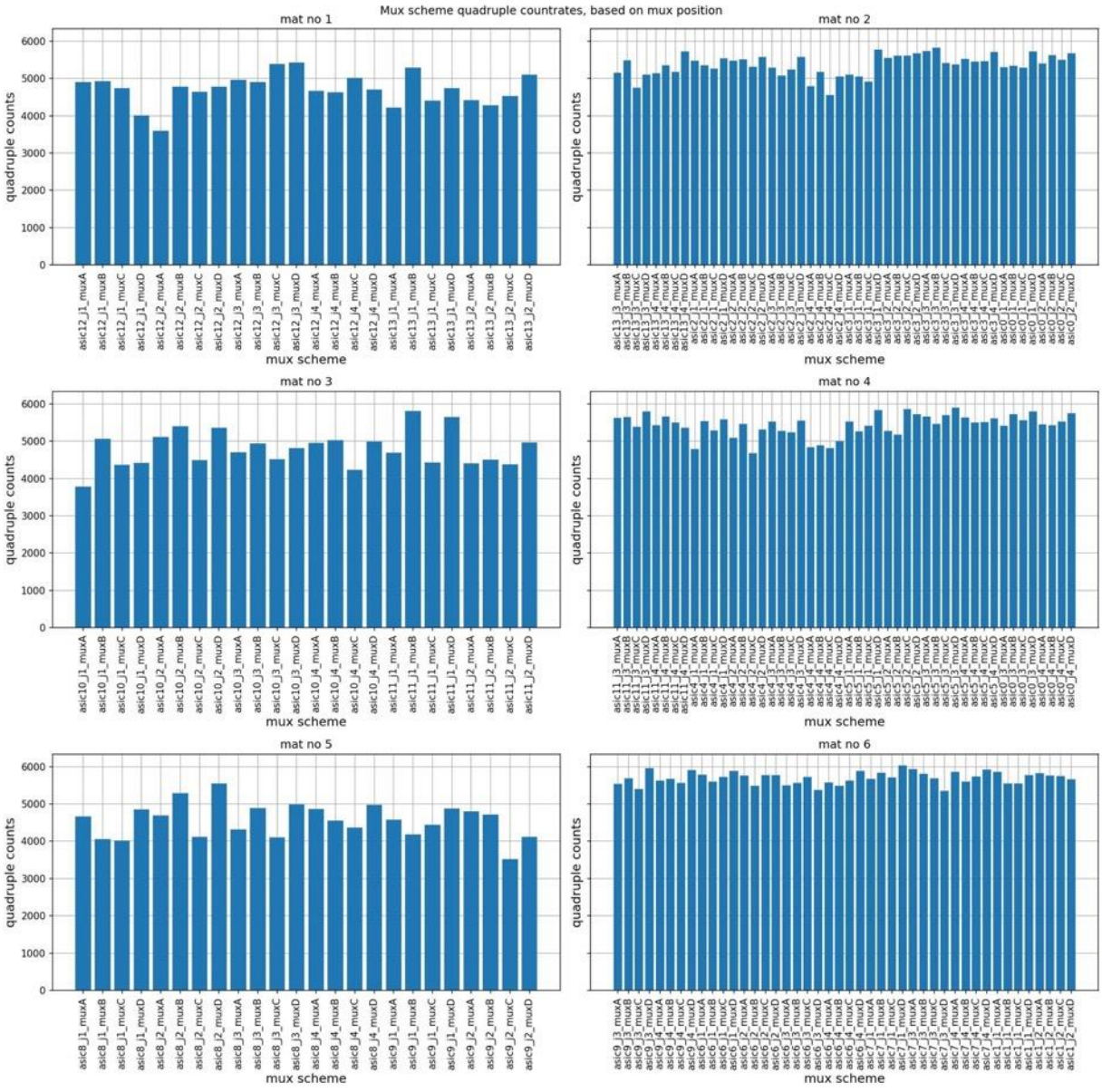

Figure 20. Multiplexing scheme quadruple count rates, based on MUX position.

replaced. In Figure 20, long fibre-mat results are presented in the left column and wide fibre-mat results presented in the right column.

3.2.3 Particle tracking and filtering

As expected, most of the internal scattering angles θ ended up between 0 and 1 degrees, indicating measured muons as shown in figure 13. These can be used for reconstruction.

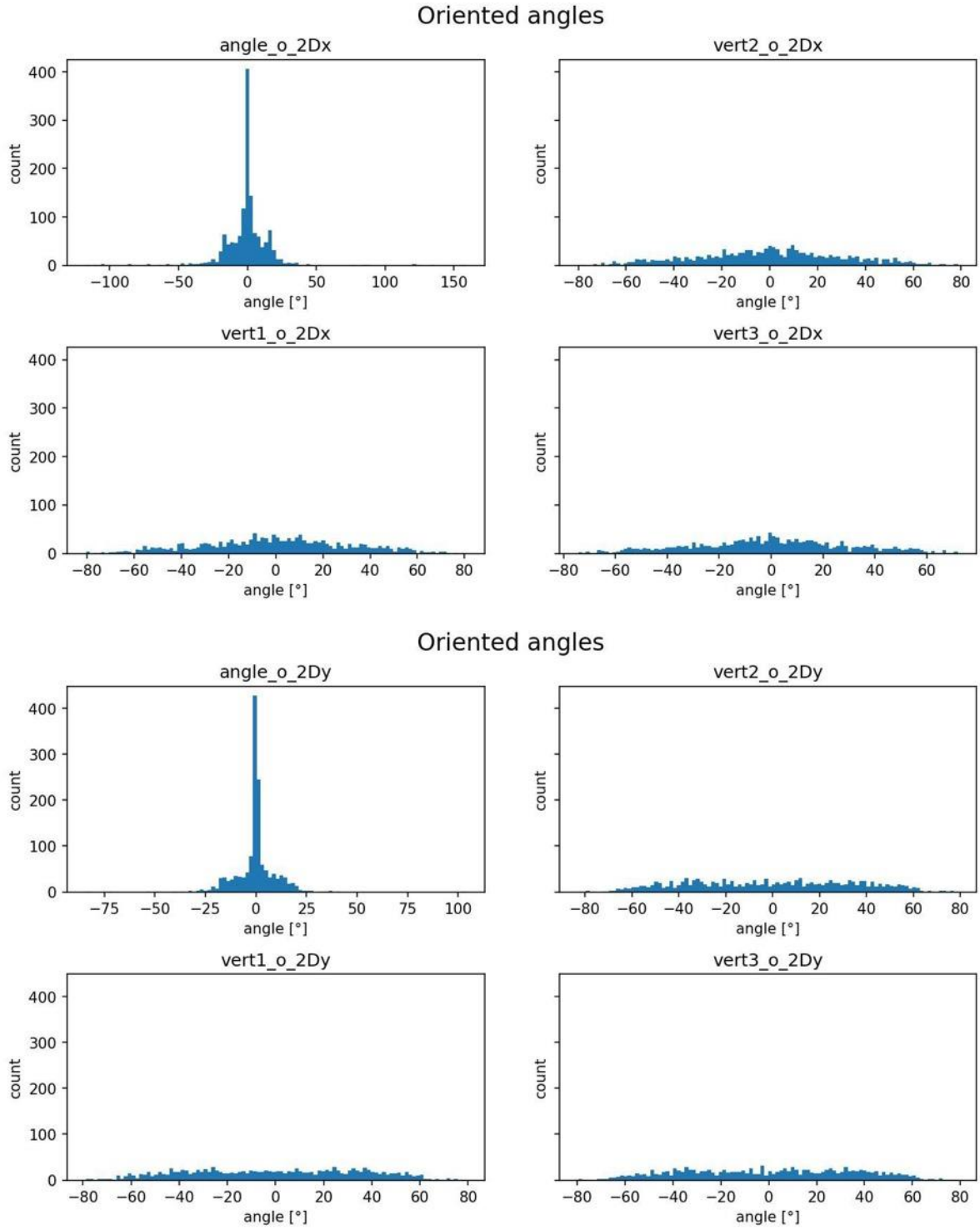

Figure 21. X and Y coordinates distribution between different fibre-mats (duration 11% of the test2_single 30 min run — 198 seconds). 2Dx and 2Dy are 2 dimensional subsets. **vert1**: angle to the normal between 1st and 2nd mat; **vert2**: angle to the normal between 2nd and 3rd mat; **vert3**: angle to the normal between 1st and 3d mat (order of mats in 2-dimensional subset). **Angle** is the angle between line connecting 1st with the 2nd mat/plate and the line connecting 2nd and 3rd mat/plate (same as int. scattering angle θ).

3.2.4 Reconstruction

In figure 22, an angular distribution of particles scattering within the hodoscope is presented. As mentioned before, the muons used for reconstruction are mostly in the <1 degree bin.

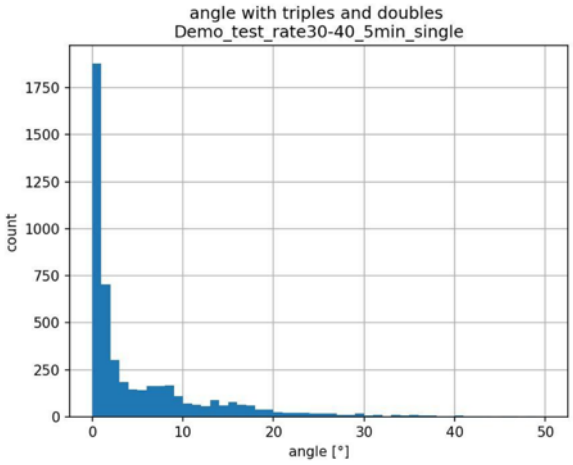

Figure 22. Angular distribution of particles scattering within the hodoscope. 1 bin =1 degree. Muons mostly in < 1deg bin, countrate at 70 muons per second.

Real life proof-of-concept reconstruction experiments were thereafter carried out by placing a lead brick of the same dimensions as in the simulation on top of ALARA's hodoscope (figure 14). As it can be seen in Figure 23, the lead brick is not yet clearly visible as the exposure time is rather short (180 min) and thus the contrast of the 2D cross-section is low.

An additional experiment was carried out by placing the lead blocks into a shape of "G". Exposure time was 60 minutes. The lead blocks are visible in different angular distribution ranges for scattering within the hodoscope.

For the second hodoscope two lead bricks were placed side by side. Exposure time was 60 minutes.

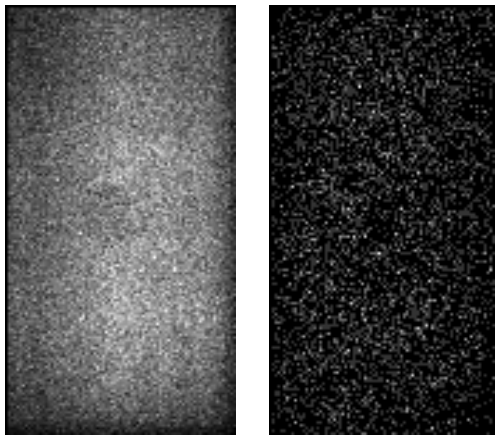

Figure 23. On the left, a physical and on the right a GEANT4 simulation of hodoscope short exposure (3 h) measurement 2D cross-section result of a lead brick.

Despite the low visual contrast, for muon tomography, these are superb results and our algorithms can clearly filter and thereafter differentiate the detected objects.

In general, based on the long exposure simulations, we have high confidence that by increasing the exposure times, we are able to increase the contrast of the data received from the exposures and thus increase the confidence results of final measurements.

First on-site measurements are to give us more information on how much time is needed.

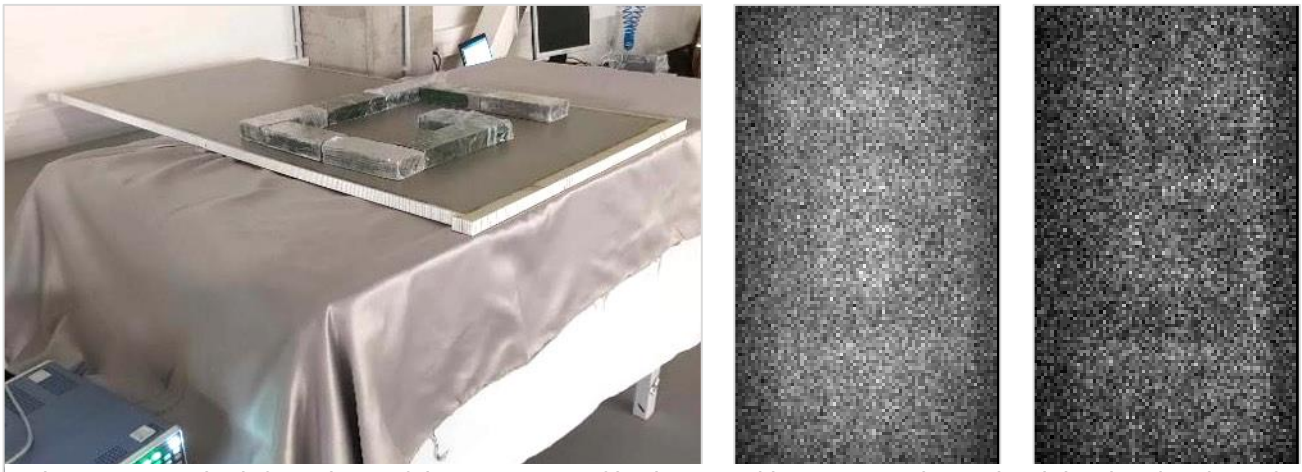

Figure 24. On the left, a photo of the test setup of hodoscope (detector No 1). On the right, density plots of number of tracks through a voxel for different particle scattering regions (0-0.6 deg muon range and 0.6-6 deg mixed range, respectively. The reconstruction pictures displayed are slices where voxel size is 1 cm.

Figure 25. The reconstruction of test exposure of the second hodoscope (detector No. 2.) with different filtering ranges. Voxel size 1 cm. Two lead bricks were place side by side and exposure time was 60 minutes.

4. 4. ON-SITE MEASUREMENTS

4.1 346A REACTOR

The 346A reactor has two entrances to Front and Back sections (see Figure 26). The main challenge is to get the hodoscopes inside and laid on the floor (as could be seen in Figure 10). Therefore, no additional details can be attached outside of the measurement areas. The area of the Front (incl. support beams) is around 6.2 x 7.3 m with an average operational height of just 0.53m. The area of the of the Back is around 2.5 x 9.5 m.

The Front has about 2 m whereas the Back only has about 0.6 m wide area where one can stand up in case mounting operations need to be carried out. Lights, electricity and most possibly an Ethernet connection are only available in the big corridor leading up to the Front entrance. Other areas need portable (wired) flood lights for lighting.

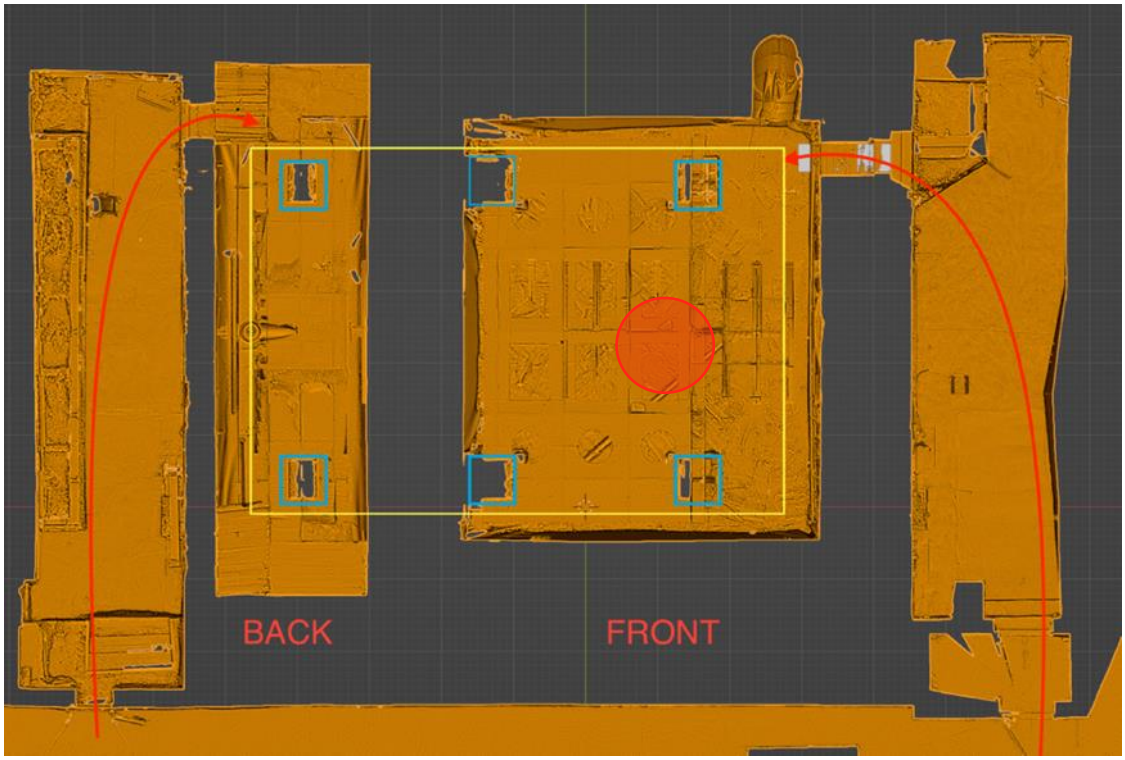

Figure 26. Top view of the 346A reactor 3D model with the entrance paths to the back and the front section marked with red arrows, support beams (ca 720 x 720 mm) marked with blue squares and the approximate location of the reactor on top indicated with the yellow rectangle (not true to its actual size). Notice the inaccessible areas (for the hodoscopes) between the support beams and the walls in addition to the “dead space” between the Front and the Back area. In these inaccessible areas the hodoscopes need to get as close as the wall as possible and measure for longer periods.

While the average radiation flux underneath the reactors is just a couple of times higher than the average natural flux (i.e., safe for medium periods), the middle of the Front area has a spot with higher radiation flux than the natural flux outdoors (see the red circle in Figure 26). This means it is highly recommended not to stay under that spot for an elongated time in order to reduce the yearly dosage a person can withstand. For safety purposes, every person will get his active personal dosimeter that will beep if the flux is too high or collected dose will exceed 10 µSv. Despite this, working underneath the reactor is feasible and it is highly likely there is a real need to access these areas for positioning setup.

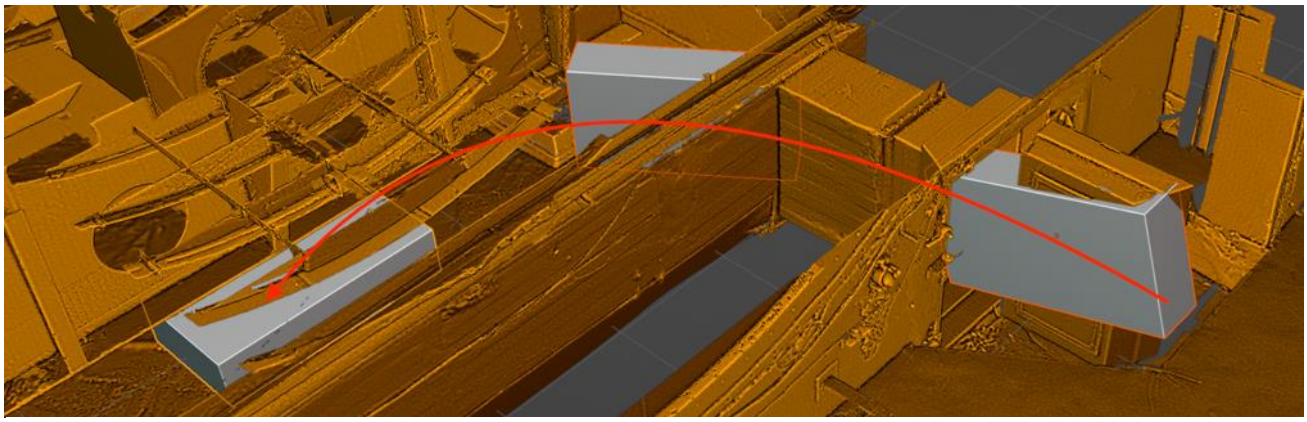

Figure 27. Process for guiding the hodoscope (in this case 1710 x 910 x 390 mm) underneath the 346A reactor. The measurements of the reactors are carried out by analysing muon tracks that have passed the reactor and then the hodoscope.

The 346A reactor has a very uneven concrete floor surface, which increases the challenge of relocating the hodoscope under the reactor. As the reactor has been in use for a longer period, it might be also referred to as the Old reactor.

4.2 346B REACTOR

The 346B reactor has a smoother concrete floor surface.

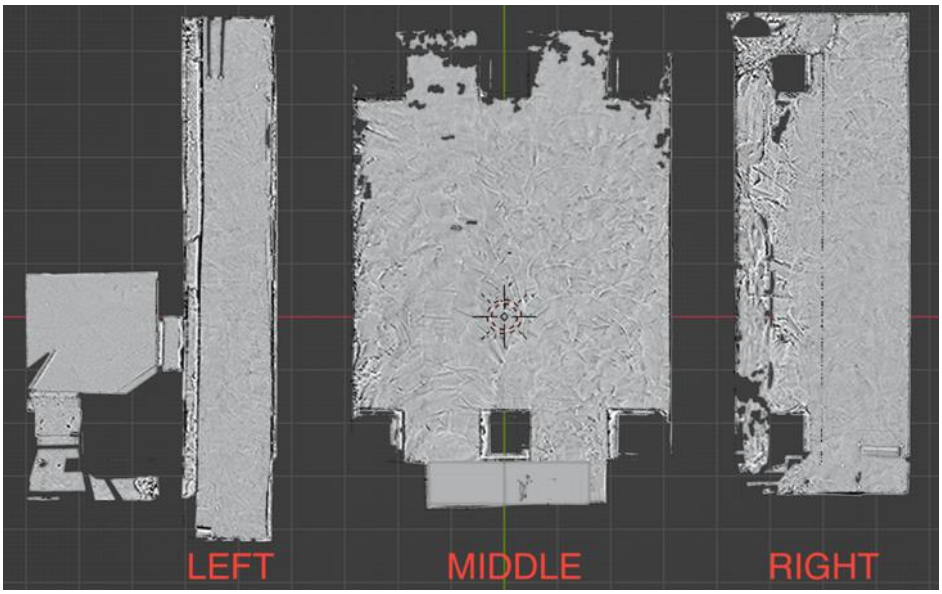

Figure 28. The 346B reactor can be accessed from 3 places: Left, Middle and Right. Although we currently assume exposures done in the Middle are sufficient, there might be a need to do exposures in the lateral sections as well. At minimum, this would require demolition works in the Right section due to even lower working area of around 0.25 m.

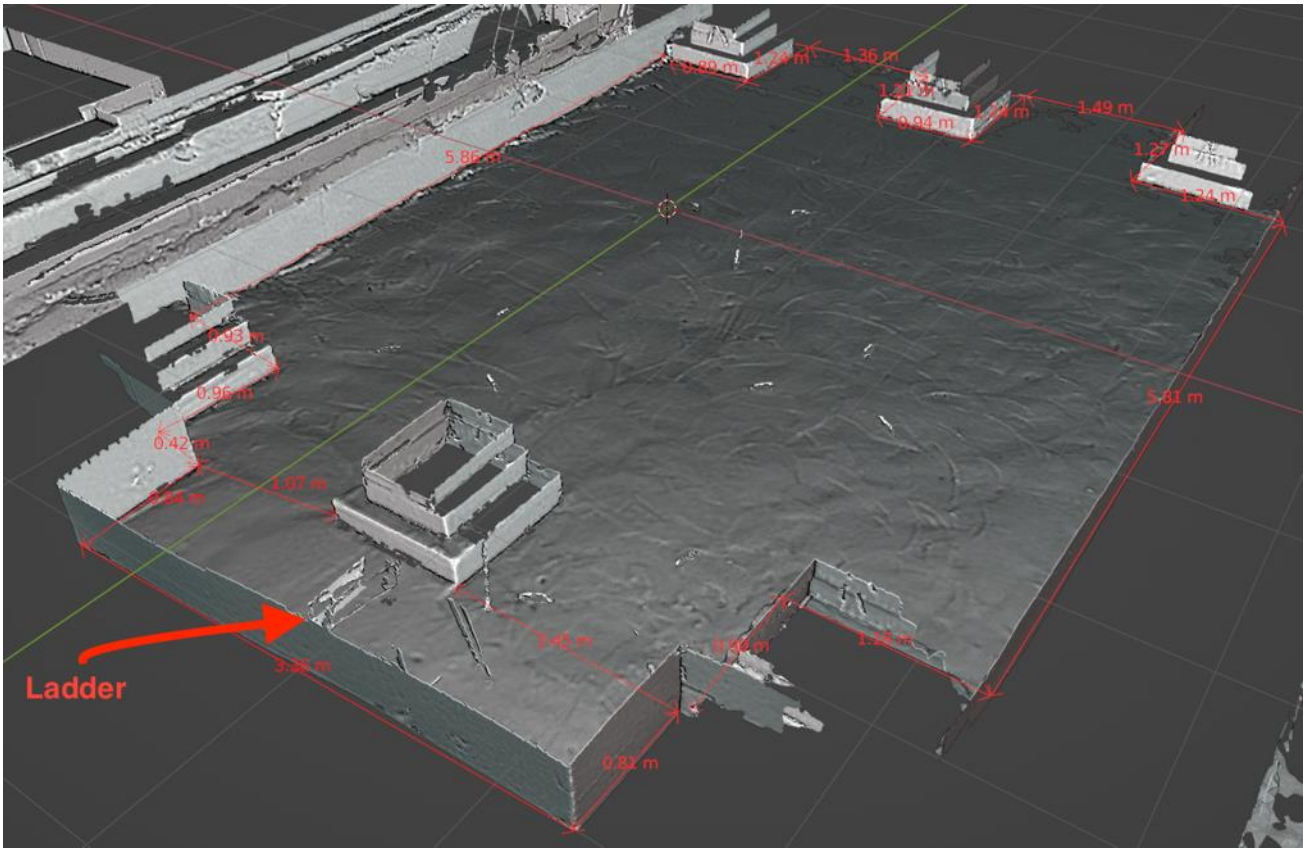

Figure 29. 346B reactor Middle section floor dimensions. This section can be accessed by a ladder.

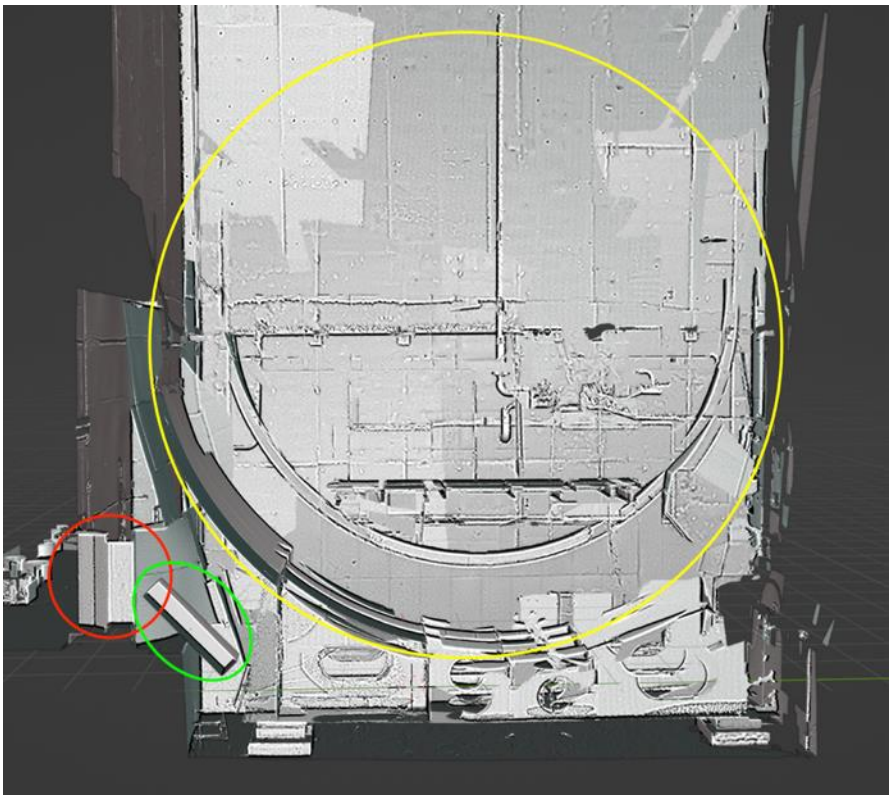

Figure 30. Scale of the entrance (marked with red), a hodoscope (marked with green) in comparison to the 346B reactor (marked with yellow). The reactor area seems hollow due to the 3D reconstruction method.

4.3 MEASUREMENT PLAN

With each reactor, the hodoscopes will do the exposures on one spot (position) after which the hodoscopes will have to be repositioned, levelled and the location saved, so the cycle could repeat in order to cover as much (active) area with the hodoscopes underneath the reactors as possible (see Figure 31, where minimum number of positions are shown). Notice

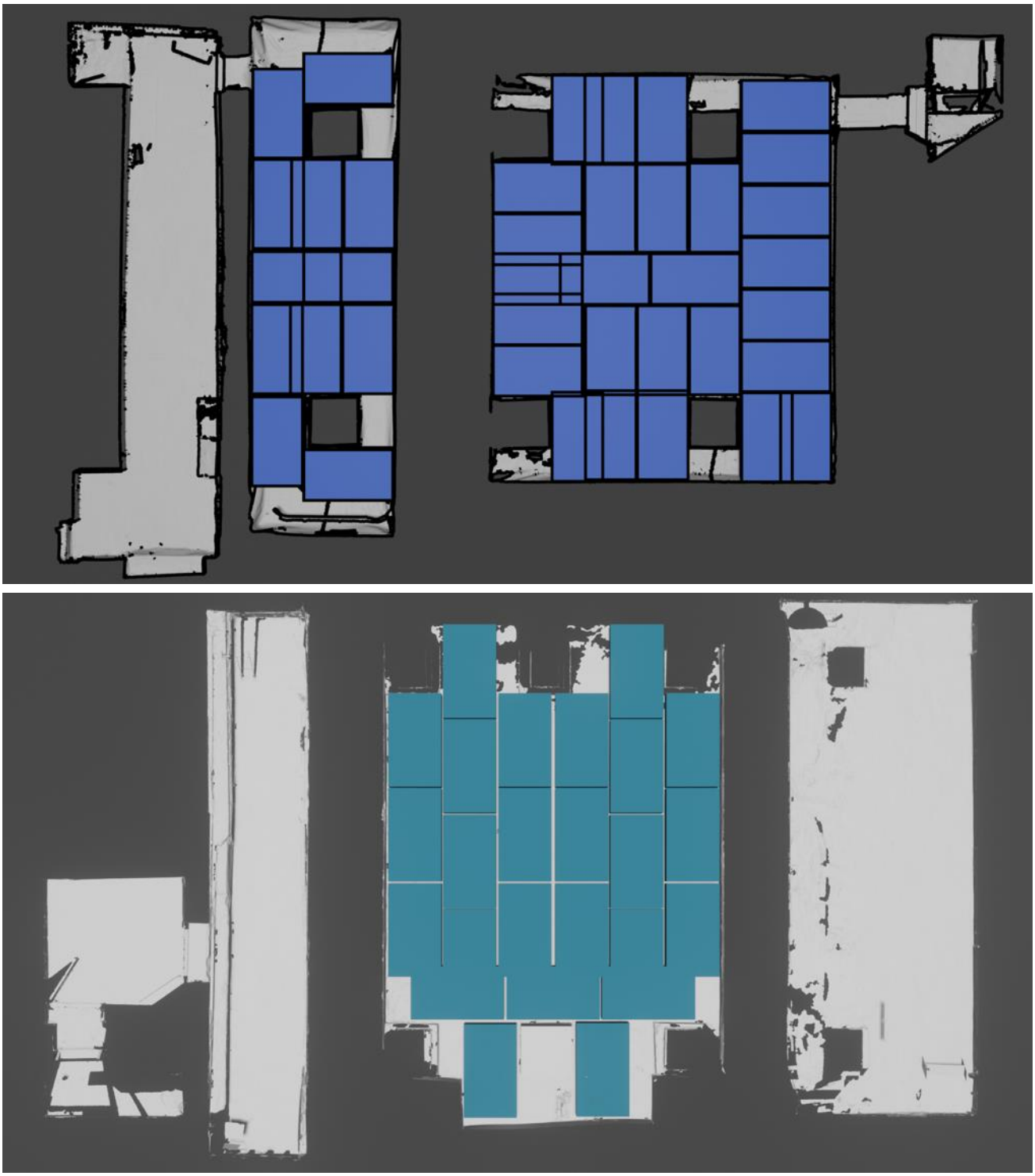

Figure 31. Above, measurement plan of the 346A reactor, where 39 different hodoscope exposure positions have been indicated. Below, measurement plan of the 346B reactor, where 25 different hodoscope exposure positions have been indicated. This is considered as the minimum measurement plan.

that there is not enough space to place the hodoscope in some areas (e.g., near the foundation posts), thus the exposure time is increased near those areas.

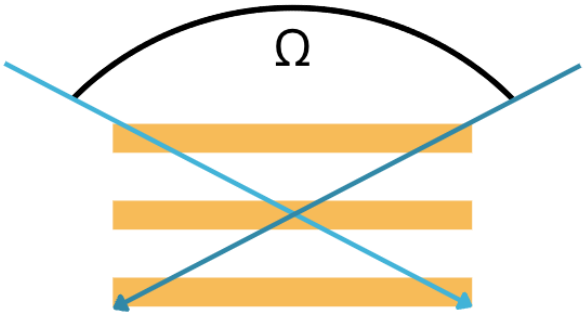

Figure 32. Schematic of the hodoscope's maximum field of view (FoV or solid angle) Ω.

Furthermore, despite these seemingly "blind spots", the reactor is mostly "visible" to the hodoscope at all times (see Figure 31) as its maximum field of view (FoV) is defined by twice the maximum angle (as measured from the surface normal) of the muon trajectory passing the hodoscope. The exposure time around these "blind spots" is increased to improve normalising the measurement results (gather more statistical data of the particle trajectories).

Essentially, every position of the hodoscope produces a 3D point cloud after a 12-to-72-hour exposure, which will have its own noise. Every time the hodoscope is repositioned, we can produce a new 3D point cloud. These 3D point clouds need to be stitched together, but since this cannot necessarily be done from the information in the existing 3D point clouds (there may be noise that would confuse the algorithms), we need to know the exact position in space of the sensor (hodoscope) that measured the corresponding 3D point cloud. Therefore, the most important thing here is to fix the position of the different positions with an accuracy of at least +- 1 cm, while +- 1 mm is preferred. The distance from the wall itself does not directly provide any useful information. Every position must be registered and forwarded to our central computer taking in the measurement data, tied to the exposure done on that position. Absolute and relative dimensions can be used as long as the 1 cm (1 mm) accuracy holds up — with the latter, an anchor point/surface is used to set the starting point or surface of the position measurement.

The first on-site measurement with ALARA's hodoscope carried out at the end of March 2023 and its results help us to define the parameters for the following tomographic measurements and reliable localization mechanism. Initially, the hodoscope will be relocated manually and its position will be semi-automatically fixed with a total station to an accuracy of few millimetres. Automated solutions are currently being tested in the lab and are waiting for on-site experiments.

4.4 ANALYSIS

GScan analytical software package is written in Python. GPU acceleration is used where applicable. Software high level functional description is as follows:

Saved data files from each detector exposure position contains channel activation data from DAQ electronics and metadata with hodoscope location in space and exposure duration. Channel activation data will be interpreted into local xyz coordinates and tracking algorithm improves particle actual trajectory through hodoscope, as well removes erroneous channel activations. After tracking algorithm angle filtering is applied to remove low energy particles. All detector position exposures will be consolidated into one large virtual detector plane using hodoscope positional metadata. Based on hodoscope two first plate xyz exposures the ray is projected into space (assuming the trajectory of particle), this process is GPU accelerated.

3D density map can be presented as 3D image or 2D cross-sectional cuts/slices where voxel ray rate after normalization can be presented as pixel intensity in grayscale or coloured heatmap.

GScan has developed analytical method for edge and object detection as well machine learning based approach. Last step allows us to generate 3D scene with all detected objects and divide these into separate logical spaces. The final product is a 3D model of reactor sections with detected objects of interest, which can be viewed with freeware programs as for example eDrawings 2022. Results are to be expected by Q4 2023.

For a more detailed plan, please see Table 2 in the following page that indicates the following expected timeline. This timeline takes 20% unexpected holdups into account, which should mitigate any issues that ought to rise during our development or measurement phases.

Figure 33. First produced hodoscope in mid-March 2023 with the team behind the effort.

5. ANNEX A. EXPECTED MEASUREMENT TIMELINE

Table 2. Expected timeline for hodoscope & software development, on-site measurements, data analysis and reporting.

Work breakdown	April '23	May 2023					June 2023				July 2023				August 2023					September 2023					October 2023				November 2023				
WEEK NUMBER	*17*	*18*	*19*	*20*	*21*	*22*	*23*	*24*	*25*	*26*	*27*	*28*	*29*	*30*	*31*	*32*	*33*	*34*	*35*	*36*	*37*	*38*	*39*	*40*	*41*	*42*	*43*	*44*	*45*	*46*	*47*	*48*
Software improvement	x	x	x	x	x	x	x	x											x	x	x	x	x	x	x								
HMS — Hodoscope Movement System improvement	x	x	x	x																													
Hodoscope calibration	x	x	x																														
Transportation to Site 1 & Site 2	x		x			x														x													
Measurement at Site 1 (346A)	x	x	x	x	x	x	x	x	x	x	x	x	x	x	x	x	x	x	x														
Removal at Site 1																				x													
Measurement at Site 2 (346B)						x	x	x	x	x	x	x	x	x	x	x	x	x	x														
Removal at Site 2																				x													
Data analysis	x	x	x																x	x	x	x	x	x	x	x	x						
Reporting																								x	x	x	x	x	x	x	x	x	

6. ANNEX B. SITE ACCEPTANCE TEST (SAT)

INITIAL FIELD TEST FROM 28TH TO 31ST OF MARCH

Overview

- **Location**: The field tests were conducted at the premises of ALARA, specifically in a room below reactor 346A, which was chosen as one of the two measurement areas during the measurement period.
- **Reasons for choosing 346A**: The choice of reactor 346A was based on several factors, including the presence of power supply near the measurement area, communication facilities, and the presence of gamma radiation, among others.
- **Test duration**: The field tests took place at the end of March and lasted for several days. The initial day was dedicated to equipment preparation and setup, while the last day was for data gathering and removal of equipment.
- **Data gathering**: Data was gathered from two different measurement positions, as shown in the figure below. Around ten different measurement sessions were conducted with varying settings and sensitivity levels. The duration of each session varied from 10 minutes to 22 hours, depending on the requirements.
- **Team size**: The setup and removal of equipment required a team of 4 people, while changing the measurement positions during the tests required 2 persons.

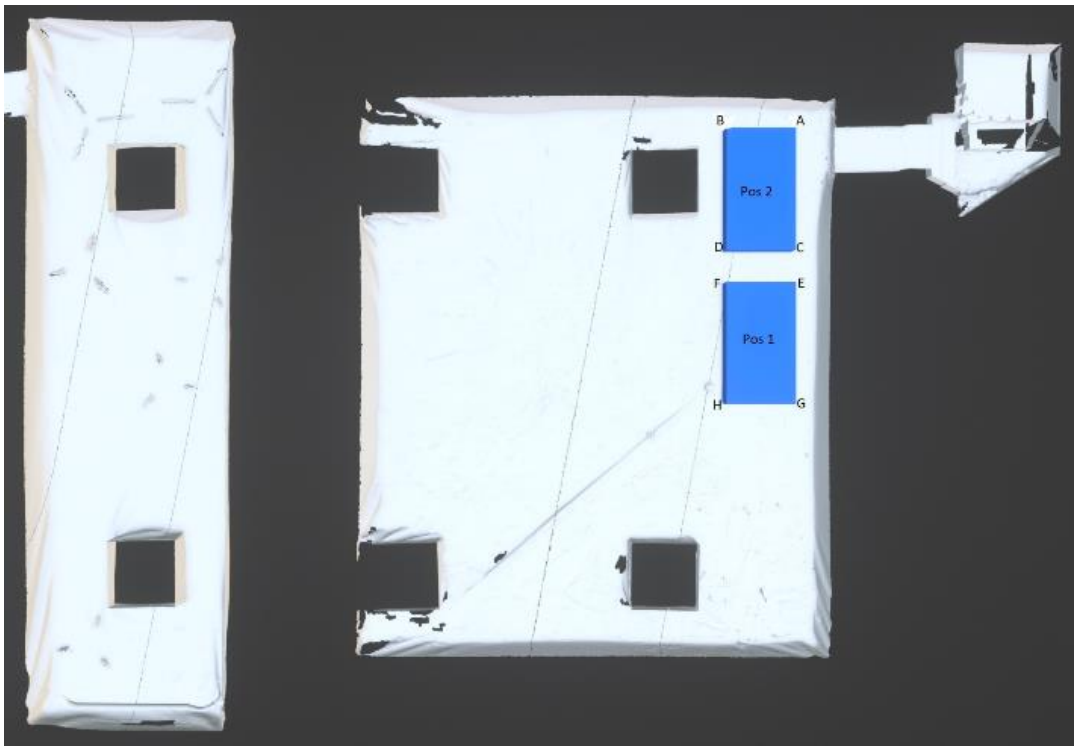

Figure 1. Layout of 346A with main entrance in the top right and two initial measurement positions — Pos1 and Pos2 — visible as dark blue rectangles.

- **Total measurements**: In total, data was gathered from two different measurement positions, and multiple measurement sessions were conducted with different settings and sensitivity levels, resulting in a comprehensive dataset for analysis and evaluation of the field test results.

Field test results, conclusion and improvement measures

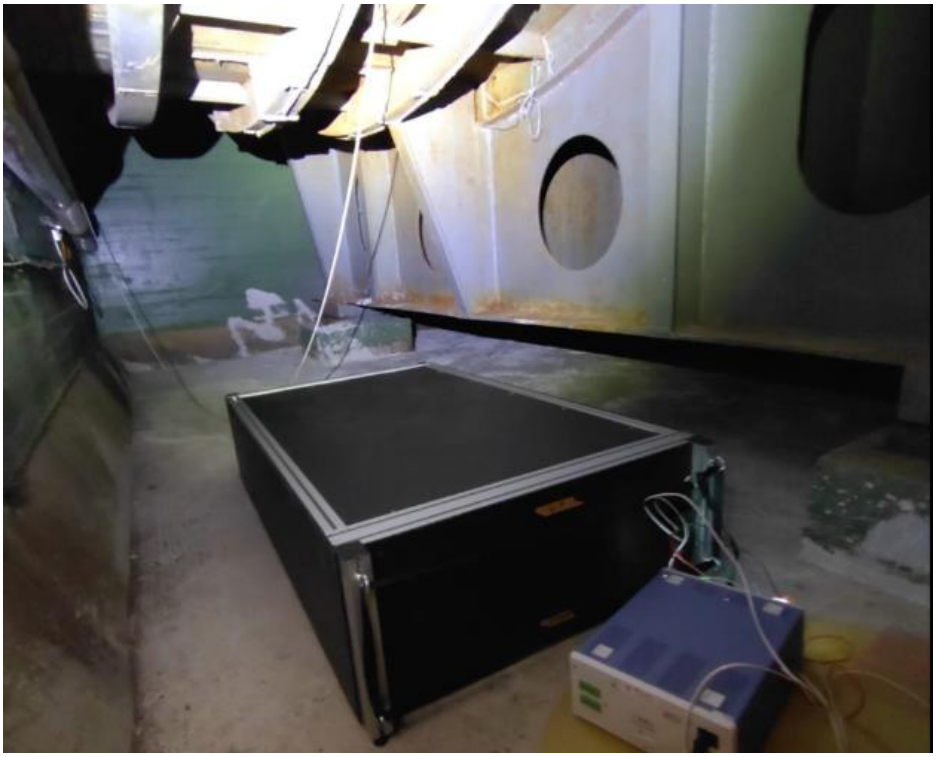

Figure 2. Hodoscope (the detector unit) in Pos1 (1st initial test position).

Based on the comprehensive data gathered and analysed during the field test conducted at the premises of ALARA, specifically at reactor 346A, we have determined that the test was successful, and all the predefined objectives were successfully achieved. The results obtained from the test provided valuable insights and confirmed the effectiveness of the ART (Atmospheric Ray Tomography) method and the SAT (Site Acceptance Test) in a reduced-scale but fully functional setup.

The test findings have significant scientific implications, including improvements in measurement procedures, reduction of operator exposure to gamma radiation, optimization of support module infrastructure, dimensioning of data acquisition and processing hardware, metadata collection and retention, specification of monitoring needs, optimization of reparative procedures, assessment of internet connectivity and quality, and identification of the need for inner sarcophagus voice communication solution. These achievements validate the reliability, performance, and feasibility of the ART in the field setting and highlight its potential for environmental monitoring and gamma radiation impact studies.